

An Experimental Study of the Flow Field and Air Distribution Strategy on a Flat Plate with Air Injection

H. Wu[†]

Department of Naval Architecture Engineering, Naval University of Engineering, Wuhan 430033, China

[†]*Corresponding Author Email: hgwuhao@126.com*

(Received November 19, 2017; accepted June 16, 2018)

ABSTRACT

In order to investigate the effect of air flow rate distribution on plate flow field characteristics, an experiment of plate with air injection was conducted in a high speed towing tank. The influence of air flow rate distribution at longitudinal and transverse on drag reduction and the morphology of air layer were investigated. The result show that the air-water mixed flow under the plate surface is mainly affected by the velocity of flow and air flow rate. When the non-dimensionalized air flow rate coefficient is less than 1.554 ($Cq \leq 1.554$), the mixed flow mainly has a bubbly flow; when the non-dimensionalized air flow rate coefficient is greater than 2.331 ($Cq \geq 2.331$), the mixed flow has an air-water stratified flow; Otherwise, there is a transitional flow that is both bubbly and stratified. The local friction drag reduction at the lower surface of the plate near the injection is 100%. The drag reduction rate of total resistance for the lower surface of flat plate will reach 60.65% when improves the strategies of air injection and the air ratio is 1:4:1 in the header air injection device. The joint air injection of header and central device has no contribution to the drag reduction rate of total resistance.

Keywords: Flat plate; Air flow rate; Distribution strategy; Drag reduction rate; Local friction

1. INTRODUCTION

The frictional resistance of large vessels is one of major resistance components, approximately 60 to 70% of the total resistance. Therefore, if a significant reduction in the frictional resistance is achieved, it will be useful in reducing carbon dioxide emissions and saving fuel costs.

Air Layer Drag Reduction (ALDR) techniques can reduce the skin friction using air layers generated on the wetted hull surface by air injection and it is a longstanding goal of naval architects. The basic principle of air lubrication is to separate the ship hull surface from the water flow around it with a thin layer of air, skin friction on the hull will be greatly reduced (Ceccio *et al.* 2010a, Ceccio *et al.* 2010b, Latorre *et al.* 1997, Matveev. 2003).

At present, all the countries in the world are working to develop a bubble ship to achieve the goal of energy saving and emission reduction, air cavity ship (ACS) of Russia has been applied in engineering, but most of the ships are small boat (Gorachev. 2012 Sverchkov. 2007, Sverchkov. 2010).

ALDR has not been applied widely to the large vessels. Some technical issues should be resolved

including: how can a stable air layer form and be maintained on the bottom of the ship, does the air layer persists enough distance, and how to improve the effect of air layer drag reduction. Sanders and Elbing conducted a set of experiments to investigate the phenomena of skin-friction drag reduction in a turbulent boundary layer at the US Navy's William B. Morgan Large Cavitation Channel. Drag reduction was achieved by injecting air from a line source through the wall of a nearly zero-pressure-gradient turbulent boundary layer that formed on a flat-plate test model with 12.9m long and 1.0m wide. The result shows that the air layer would form on the bottom of the flat-plate and persist along its entire length at lower flow speeds and higher air injection rates. Such air layers lead to skin friction reduction of greater than 80% (Sanders *et al.* 2006, Elbing *et al.* 2008, Elbing *et al.* 2013). Zverkhovskiy design a series experiments with a flat plate (2m in length and 0.298m in width) in the cavitation tunnel at the ship hydromechanics group of the Delft University of Technology. The test results show that the use of air cavities can make the drag reduction up to 60% and the number cavities can be optimized for specific flow conditions in order to maximize the drag reduction (Zverkhovskiy *et al.* 2012, Zverkhovskiy *et al.* 2013). Watanabe (Watanabe *et al.* 1998), Kodama

(Kodama et al. 1999) and Kazuhiro (Kazuhiro et al. 2000) have performed experiments with long slender flat-bottom ship model, ranging from 5.5m to 22m. Air was injection from the bottom of the test model. The result shows that the drag reduction was decay with downstream distance and only slight drag reduction existed by the end of the test model.

In this paper, the authors developed high precision total resistance and local friction force sensors first, and then the air layer observation system with large scale plate is established in a towing tank. A complete air layer drag reducing test methods is formed, and the main factors affecting the air layer drag reduction has also been obtained. What is more, the influence of air flow distribution at longitudinal and transverse on drag reduction and the morphology of air layer were investigated. The research work of this paper can provide technical support for air layer drag reduction test in the future.

2.EXPERIMENTAL SETUP

2.1 Test Model

The experiments were conducted in the towing tank of the Chinese Special Vehicle Research Institute, which is the longest towing tank in China. The towing tank is 550m long, 6.5m wide, 5.0m deep, and equipped with a drive carriage facilitating shipped of 0 to 15 m/s for test.

The test model, shown schematically in Fig. 1, was a rigid flat plate (5.02m long, 1.00m wide and 0.12m thick). Its leading and trailing edge are carried out by the NACA0015 airfoil, and the middle part is parallel medium body. The test surface of the model faced downward so that gravitational buoyancy forced bubble toward the test surface. The experimental x-axis begins at the model's leading edge and increase in the downstream direction. The y-axis is normal to the test surface defined by $y=0$, and increases with the depth of water. The z-axis runs span wise, a right-handed coordinate system.

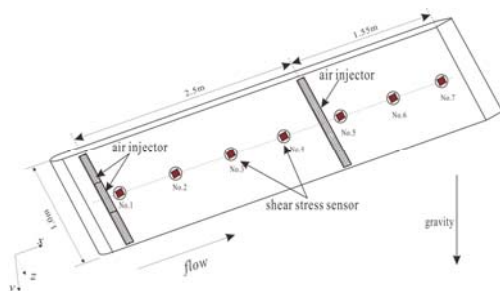


Fig. 1. Sketch map of the test model

In order to investigate the effect of longitudinal and lateral air flow distribution on the drag reduction, two air jet plates are installed on the surface of the plate at the fixed location $x=0.466m$ and $x=2.966m$. The air flow was controlled by connecting pipes and air injector at different locations.

To explore the air injection impact on local friction

of different locations, the spatially average wall shear stress, $\tau_w = D_f / A$, was determined from seven floating-plate strain-gauge force balances that measured the skin friction drag force, D_f , on a square flush mounted surface of area A having a $25cm^2$. These sensors were fabricated well, and were all located at the same span wise location at $x=0.66m, 1.31m, 1.96m, 2.61m, 3.26m, 3.91m,$ and $4.56m$.

2.2 Instrumentation

2.2.1 Air injector

Air was injected through the lower surface of test model at two locations, $X_{inject}=0.466m$ and $X_{inject}=2.966m$. Each location has three separate air injector device. The design of the air injector device is shown in Fig. 2. Each air injector device consists of four parts:

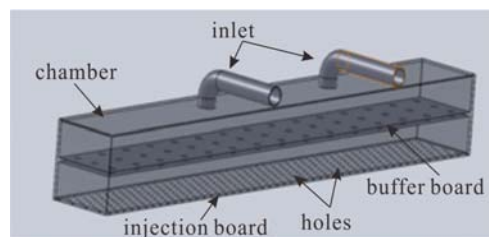


Fig. 2. Design of the air injector device

two inlets, chamber, buffer board and injection board. Air jet holes with an aperture of 2mm are arranged on the injection plate. The width of the air injector device is about 0.29 m. Each air injector device is set up two inlets, which connected to an air tube by a T-junction, and the air tube was connected to the air supply system. The function of the buffer plate is to make the air uniform. There are totally 6 air supply pipe, each air pipelines are set up with switch and flow control devices.

2.2.2 Flow Metering

Figure 3 shows the glass rotor flow meter. The air injection rate was monitored using several flow meters (LZB-40 and LZB-50) mounted at the center of 1.5cm inner diameter pipes. In order to ensure the flow was fully developed at the monitoring locations, the flow meters were located at every line junctions. The flow meters were factory calibrated for the range of 0-240 SCFM (Standard cubic foot per minute) at the test temperature.



Fig. 3. Glass rotor flow meter

2.2.3 Local Skin-Friction Force Sensor and Single Force Sensor

Figure 4 shows the local skin-friction sensor and the single force sensor. Local skin-friction measurements were made at seven stream wise locations using floating-plate-type drag balances. These sensors were fabricated in air and water well. The floating plates were fixed rigidly to beryllium copper flexure that was instrumented with a full Wheatstone bridge of semiconductor strain gauges. The skin-friction balances were calibrated from 0-5.0N. The loads were applied to the floating plate via a suction cup. The precision load cell was calibrated in the vertical position using laboratory weights prior to its use. Multiple calibrations were performed on the skin-friction sensors to confirm their repeatability and to assess their uncertainty. The measurement uncertainty was typically $\pm 0.6\%$. The single force sensor is used to measure the total resistance of plate in the water. There are two single force sensors that fixed on the upper surface of the plate. The sensors were calibrated from 0-500N.

2.2.4 Air layer observation system

Air layer observation system includes land-based shooting device and underwater camera. In the fixed position of the bottom of the towing tank, the underwater light source and underwater imaging system are arranged in real time to capture and record the morphology of air layer at different conditions. Figures 5~6 shows the land-based shooting device and underwater camera.

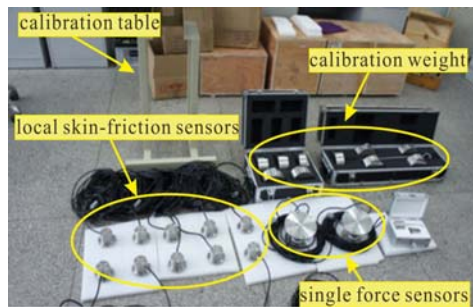


Fig. 4. Local skin-friction sensor and single force sensor



Fig. 5. Land-based shooting device

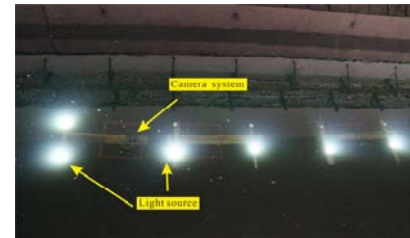


Fig. 6. Underwater camera

2.3 Model Install

Figure 7 shows the installation of the test model. The experimental model is fixed by double struts, which is connected with the trailer by the telescopic navigation mechanism. The depth of flat plate to water surface can be smooth adjusted though the compass of the navigation system. In order to reduce the interference of navigation mechanism and flow field of plate, two streamlined shroud were installed outside the struts, and the gap between the end of shrouds and test model is reserved for 10mm. The lateral position of the strut is located in the longitudinal section of the plate, and the center axis of the vertical axis is symmetrically arranged, the center line of the front strut is $x=1.02\text{m}$, and the center line of the post is $x=3.62\text{m}$. The pillars and the test model were connected by two single sensors.

The velocity of the plate was controlled by the trailer and air flow rate was monitored by the glass rotor flow meter. Morphology of the plate bottom air layer was record by air layer observation system. The total resistance of the plate was measured by two single force sensors and local friction at a specific location of the plate is measured by the local skin-friction force sensors.

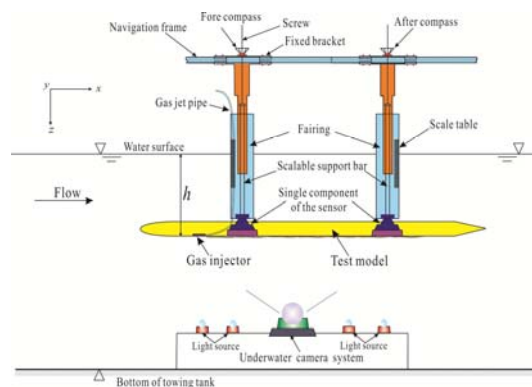


Fig. 7. Installation of test model

3. FORM OF AIR LAYER AND ITS INFLUENCE FACTORS

When the air is directly injected into the surface of the plate, the gas-liquid mixture flow is formed. The morphology of the gas liquid mixed flow presents three kinds of forms along with the change of air flow rate and speed: (a) Bubble, the air is separated into bubbles and moved backward to the surface of the plate. (b) Transitional Air Layer, partially broken bubble into air layer, other air is still in the form of the bubble to move backward (c) Developed Air Layer, all bubbles are aggregated together, and a continuous layer covers the entire surface. A schematic diagram of the typical form of the surface mixed flow under the plate is shown in Fig. 8.

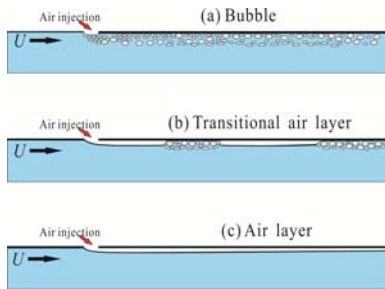


Fig. 8. Typical form of mixed flow

The morphology of air layer is closely related to the air flow rate and flow velocity, and it conforms to the rules that the gas-liquid mixture flow presents bubble when the air flow ratio is low and it will form air layer when speed is low but the air flow rate is high. In other cases, the gas-liquid mixture flow presents transition air layer flow. When the velocity is constant, the lateral diffusion of air layer increases with the rising of air flow rate. However, the lateral diffusion of the air layer decreases with the rising of velocity when the air flow rate is constant.

In order to further reveal the air flow rate and flow velocity on the influence of the morphology of air

layer, definition of non-dimensional air flow rate coefficient C_q .

$$C_q = \frac{Q}{V \cdot B \cdot \delta} \tag{1}$$

Where Q is the air flow rate, V is the inflow velocity, B is the transverse width of air inject entrance, δ is the thickness of boundary layer of the air inject entrance at no air injection, which is given by Eq. (2).

$$\delta = \begin{cases} 5.2R_e^{-\frac{1}{2}}x & R_e \leq 3 \times 10^6 \\ \frac{0.0598x}{\lg R_e - 3.107} & R_e > 3 \times 10^6 \end{cases} \tag{2}$$

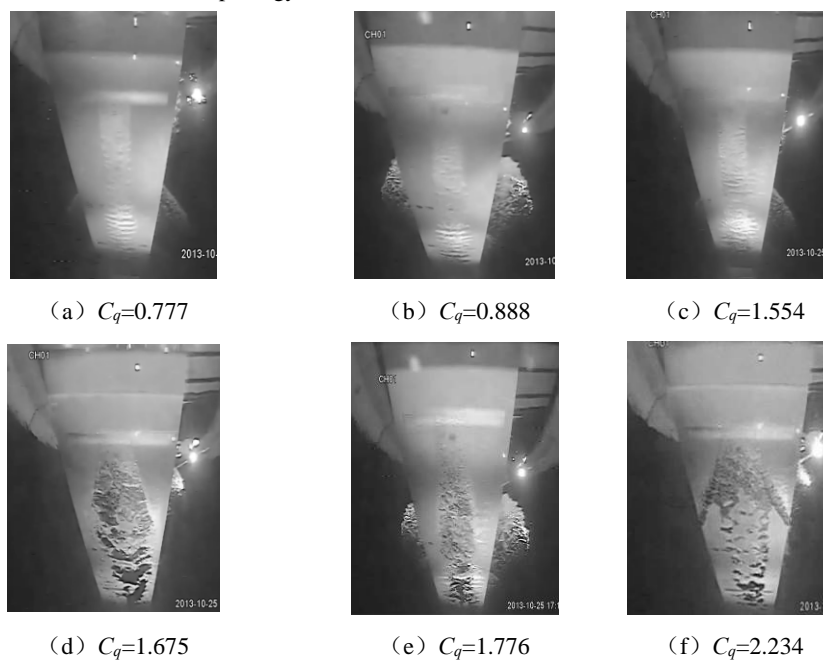
Here, Re is the Reynolds number of the air inject entrance, which is given by Eq. (3).

$$R_e = \frac{V \cdot x}{\nu} \tag{3}$$

Where x is the distance of the air inject entrance and flat leading edge, that is $x=0.3m$ in this paper, ν is the water viscosity coefficient and $\nu=1.003 \times 10^{-6}$ at normal temperature.

Figure 9 shows the morphology of air layer under the air injection of middle injector located in front of the plate. It shows that the formation of air layer is related to C_q . When $C_q \leq 1.554$, the air layer shows as a bubbly flow; when $C_q \geq 1.675$, it turns to transitional air layer flow and it transforms to air layer stratified flow when $C_q \geq 2.331$.

Figure 10 shows the morphology of air layer under the air injection proportion of 1:1:1 by the three injectors located in front of the plate. Comparison Figs. 9 and 10, it can be found that a larger surface area will be covered with air layer and the air layer is uniform when the three air injectors devices work simultaneously.



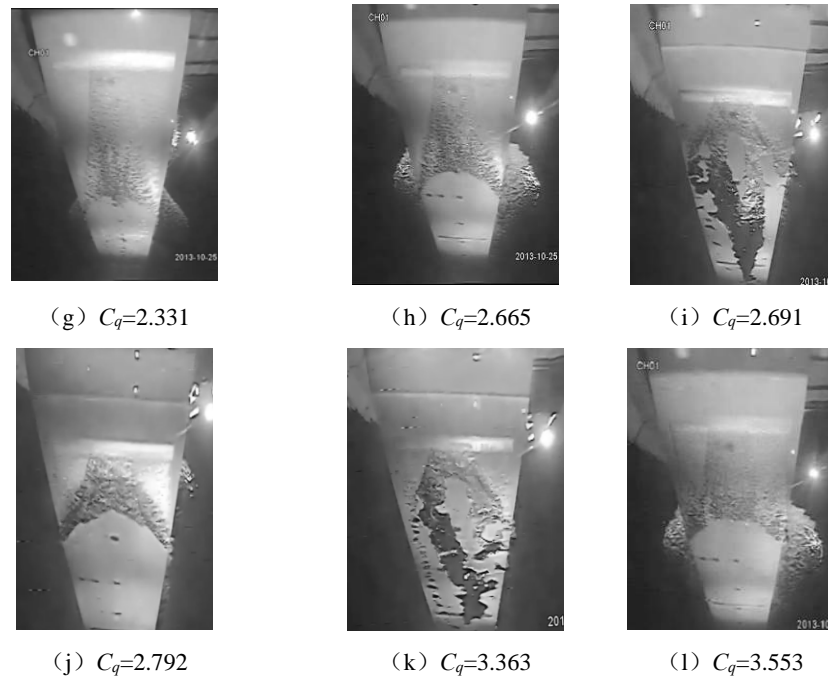


Fig. 9. Air layer shape of the header air injection with the proportion of 0:1:0

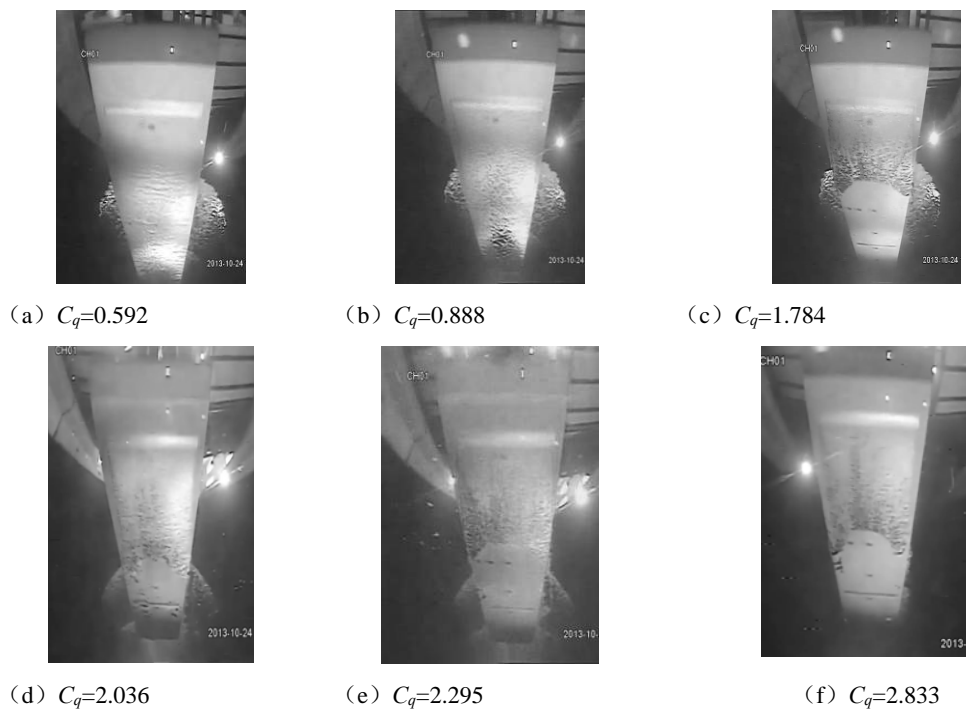


Fig. 10. Air layer shape of the header air injection with the proportion of 1:1:1

4. Resistance performance and its influence factors

4.1 Definition of drag reduction rate

The speeds for this experiment have been calculated based on the Froude law as follows:

$$Fr = \frac{v}{\sqrt{gl}} \quad (4)$$

Where Fr is the Froude's number, v is the speed of plate, g is the gravity acceleration and l is the length of plate.

In order to clearly reflect the influence of the parameters on the resistance of the plate, the drag

reduction rate of the bottom surface of the plate is as follows:

$$\eta = \frac{R_b - R_b^{\text{air}}}{R_b} \quad (5)$$

Where R_b is the resistance of bottom plate without air, R_b^{air} is the resistance of bottom plate with air.

Figure 11 shows the experimental, calculations by FLUENT and empirical formula calculations for the resistance of the plate without air in the depth of 1.0m. It can be seen that the error between the FLUENT software calculation of the total plate resistance value and the experimental value is within 4%, the resistance of the surface of the plate computing values and the empirical formula calculation error is less than 3%. The empirical formula is the formula of 1957ITTC (Larsson *et al.* 2010). In this way, the friction of flat bottom surface can be decomposed approximately.

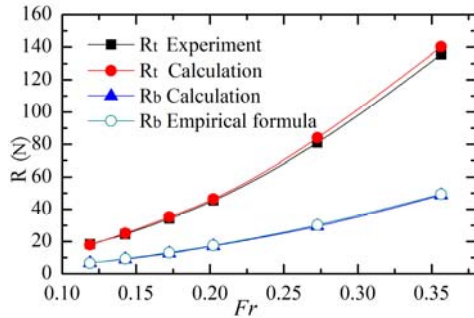


Fig. 11. Plate resistance of test and calculated at depth 1.0m

Air layer drag reduction is mainly to reduce the frictional resistance of the bottom surface of the plate and has little effect on pressure drag of the plate. Besides, it assume that the telescopic navigation mechanism in the test have no effect on the flow field around the plate. So the reduced drag (ΔR) in the experiment is the value of bottom plate friction, and $\Delta R = R_t - R_t^{\text{air}} = R_b - R_b^{\text{air}}$.

4.2 Total Resistance performance

Figure 12 gives the variation of the drag reduction rate with the air flow rate in the middle of the air injection device in the front of the plate. It can be seen that the drag reduction rate increases with increasing of the air flow rate when the inflow velocity is constant. When the air flow rate reaches a certain value, the drag reduction rate reaches the maximum, which is called the saturation air flow rate. The saturated air flow rate increases with the increasing of speed. In the test, the saturated air flow rate are $Q=10\text{m}^3/\text{h}$, $10\text{m}^3/\text{h}$, $15\text{m}^3/\text{h}$, $20\text{m}^3/\text{h}$ at the $Fr=0.119$, 0.172 , 0.272 , 0.356 . When the air flow rate exceeds the saturated air flow rate, the drag reduction rate will slightly decrease. Under the same air flow rate, the drag reduction rate decreases when the speed increases. Drag reduction rate reaches 40.34% under saturated air flow rate at $Fr=0.119$.

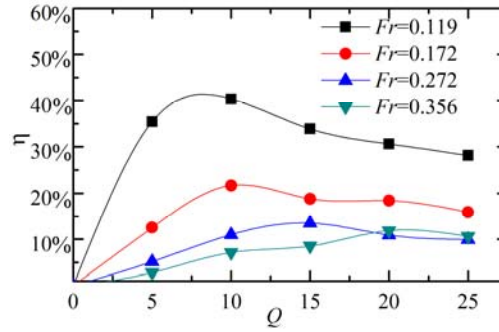


Fig. 12. Variation of the drag reduction rate with the air flow rate in the middle of the air injection device in the front of the plate

4.3 Local friction and its influence factors

There are three kinds of drag reduction methods for the three different types of flat plate mixed flow: Bubble Drag Reduction (*BDR*), Transitional Air Layer Drag Reduction (*TLADR*), and Air Layer Drag Reduction (*ALDR*). Percentage local skin-friction drag reduction %DR, is shown versus downstream distance from the injector ($X-X_{\text{inject}}$) in Figs. 13~16 for the four test speeds ($Fr=0.119$, 0.143 , 0.172 and 0.429). As shown in Figs. 13~16 that the local frictional drag reduction rate is higher in the vicinity of the injector. For the discussion of *BDR* in this paper, the local friction drag reduction rate is relatively high near the injector and then decreases rapidly to zero with downstream distance. The decreasing drag reduction with downstream distance is associated with the migration of bubbles from the near-wall region where they are effective at reducing drag. Shear-induced lift forces from the mean velocity gradients in the boundary coupled with turbulent diffusion are suspected of driving the bubbles from the solid surface resulting in poor persistence of drag reduction. Under certain conditions, drag reduction approaching 60% was achieved in the distance of 1 m of the injector. This high level of drag reduction resulted from the morphology of air layer between the test model and the liquid flow. The morphology of air layer is observed by the camera under the water of the towing tank.

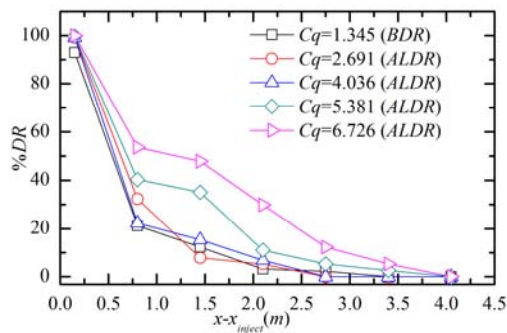


Fig. 13. Local friction drag reduction for $Fr=0.119$

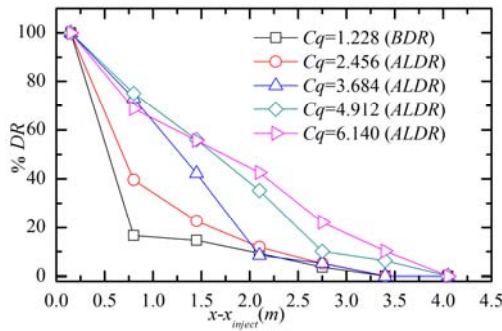


Fig. 14. Local friction drag reduction for $Fr=0.143$

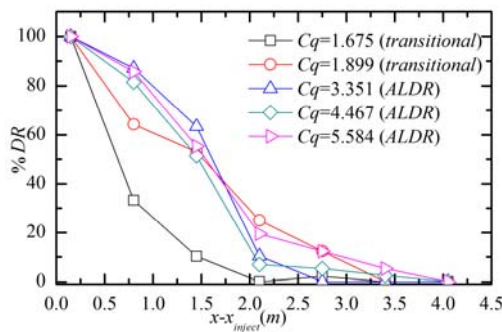


Fig. 15. Local friction drag reduction for $Fr=0.172$

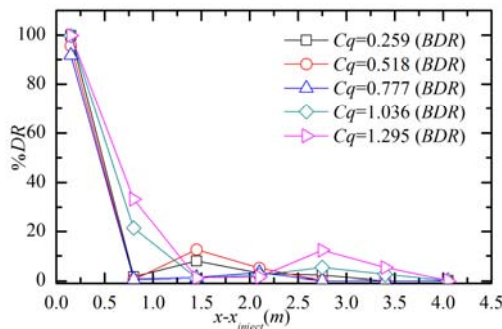


Fig. 16. Local friction drag reduction for $Fr=0.356$

5 Influence of the air injection strategy

The left and right bottom plate surface is not covered by air layer when the ratio of air injection is 0:1:0 in the header air injector. The air lateral overflow is serious when the ratio of the left, middle and right is 1:1:1. In order to investigate whether synergy occurs with nearby injection location, experiments were conducted where air was injected into the boundary layer simultaneously from the six injectors with different proportion.

5.1 Influence of air lateral distribution

Figure 17 shows the variation of the drag reduction rate with the air injection ratio in the header air injector under different speed. It can be seen that the drag reduction effect of the saturated air flow rate at each speed is better when the air injection ratio of the first device is 1:4:1 and the

drag reduction reaches 60.65% when the $Fr=0.119$.

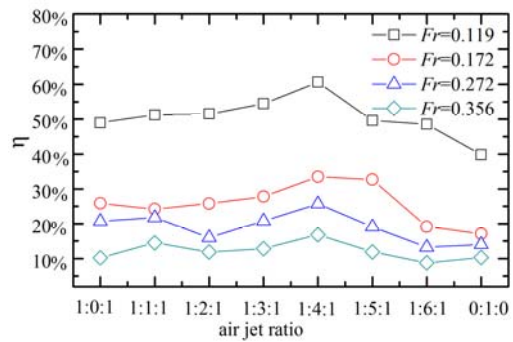


Fig. 17. Drag reduction ratio varies with transverse air flow distribution

Figure 18 shows the morphology of air layer under different lateral ratio of $Q=15m^3/h$ and $Fr=0.272$. It can be seen that the lateral diffusion of the air layer gradually increases with the increase of the air flow in the jet device, and the 1:3:1 and 1:4:1 in the jet plane is larger and the air layer is more uniform.

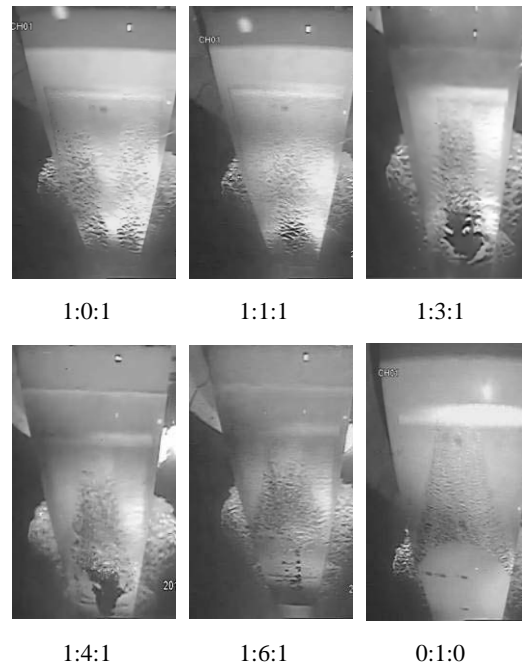


Fig. 18. Air layer at different air flow distribution scheme with $Q=15m^3/h$, $Fr=0.272$

5.2 Influence of air longitudinal distribution

The drag reduction affected by the longitudinal distribution between the header and central air injection device was carried out at the saturated air flow rate. Figure 19 shows the variation of the drag reduction rate with the longitudinal air injection ratio. It can be seen that the addition of the central air injection did not improve the drag reduction effect when the air flow rate is constant. The effect of drag reduction is the best when the header air injection device works alone (1:0), however, when the central air injection device works alone (0:1), the drag reduction effect is the worst.

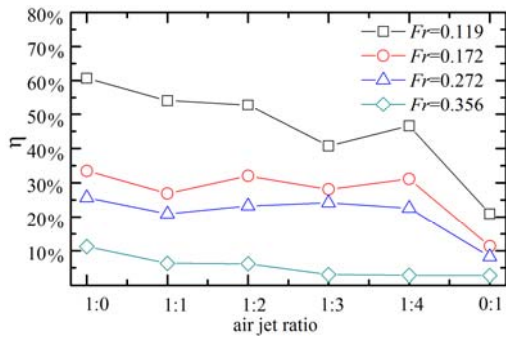


Fig. 19. Drag reduction ratio varies with longitudinal air flow distribution

Figure 20 shows the morphology of air layer under different longitudinal air injection ratios of $Q=20m^3/h$ and $Fr=0.272$, which can be seen from Fig. 20 that the coverage of the flat panel is reduced with the increase of air flow rate in the middle part of the air injection device. No stable air layer was formed when the air flow rate was split evenly between the two injectors, the drag reduction decayed drastically, even if the total air flow rate was larger than the single-injector at the leading edge. These results indicated that there are no synergistic effects of compound injection that improve efficiency.

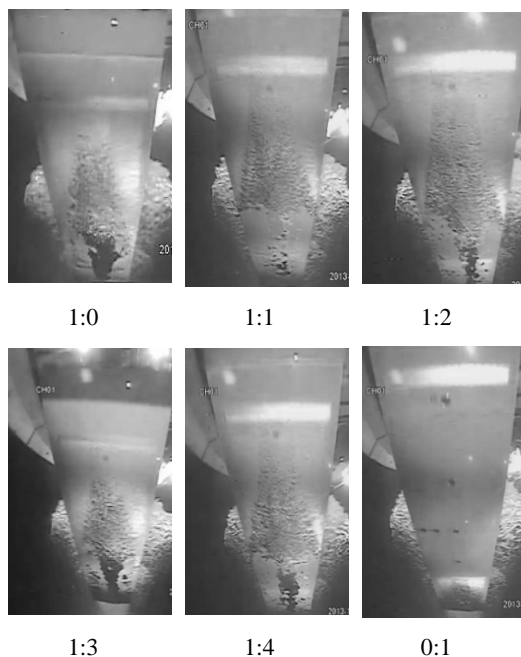


Fig. 20. Air layer under the joint air injection of header and central device

6. Discussion and conclusion

(1) Air-water mixed flow under the plate surface is mainly affected by in flow speed and air flow rate. When the non-dimensionalized air flow rate coefficient is less than 1.554 ($Cq \leq 1.554$), the mixed flow mainly has a bubbly flow; when the non-dimensionalized air flow rate coefficient is greater than 2.331 ($Cq \geq 2.331$), the mixed flow has

an air-water stratified flow; Otherwise, there is a transitional flow that is both bubbly and stratified.

(2) The local friction drag reduction rate is 100% in the vicinity of the injector. For the current discussion of BDR, the local friction drag reduction rate is relatively high near the injector and then decreases rapidly to zero with downstream distance. But, for the ALDR, under certain conditions, drag reduction approaching 60% was achieved in the distance of 1 m of the injector. This high level of drag reduction resulted from the formation of an air layer between the test model and the liquid flow.

(3) The drag reduction will reach 60.65% when improve the strategies of air injection and the air flow ratio is 1:4:1 in the header air injection device.

(4) There are no synergistic effects of longitude compound injection that improve efficiency of ALDR over the range of parameters investigated.

Acknowledgments

This research is supported by the Ministry of Industry and High Technology Marine Scientific Research projects (Grant No.[2011]530), High Performance Marine Technology Key Laboratory of the Ministry of Education Open Fund (Grant No.2013033102).

REFERENCES

Ceccio, S. L. (2010a). Frictional drag reduction of external flows with bubble and gas injection. *Annual Review of Fluid Mechanics* 42,183-203.

Ceccio, S. L., M. Perlin and B. R. Elbing, (2010b). A cost-benefit analysis for air layer drag reduction. *International Conference on Ship Drag Reduction SMOOTH-SHIPS, Istanbul, Turkey.*

Elbing, B. R., E. S. Winkel, K. A. Lay, S. L. Ceccio, D. R. Dowling and M. Perlin (2008). Bubble-induced skin friction drag reduction and the abrupt transition to air-layer drag reduction. *Journal of Fluid Mechanics* 612, 201–236.

Elbing, B. R., S. Makiharju, A. Wiggins, M. Perlin, D. R. Dowling and S. L. Ceccio (2013). On the scaling of air layer drag reduction. *Journal of Fluid Mechanics* 717, 484-513.

Gorachev, Y. N. (2012). Drag reduction induced by the addition of a multi-cavity-challenges and successes, *ATMA*.

Kazuhiro, F. and J. Junichiro (2000). Frictional drag reduction with air lubricant over a super-water-repellent surface. *Journal of Marine Science and Technology* 5,123-130.

Kodama, Y., A. Kakugawa and T. Takahashi (1999) Preliminary experiments on microbubbles for drag reduction using a long flat plate ship. *ONR Workshop on Gas Based Surface Ship Drag Reduction*, 1–4.

- Larsson, L and H. C. Raven (2010). The principles of naval architecture series ship resistance and flow. *Society of Naval Architects and Marine Engineers*.
- Latorre, R. (1997). Ship hull drag reduction using bottom air injection. *Ocean Engineering* 24(2), 161-175.
- Matveev, K. I. (2003). On the limiting parameters of artificial cavitation. *Ocean Engineering*, 30, 1179-1190.
- Sanders, W. C., E. S. Winkel, D. R. Dowling, Perlin M. and S. L. Ceccio (2006). Bubble friction drag reduction in a high-Reynolds-number flat-plate turbulent boundary layer. *Journal of Fluid Mechanics* 552, 353–380.
- Sverchkov, A. V. (2007). Potential of the artificial air cavity technology for raising the economic efficiency of china's inland waterway shipping[C]. *Ninth international conference on fast sea transportation, Shanghai, China*.
- Sverchkov, A. V. (2010). Application of air cavities on high-speed ships in Russia. *International Conference on Ship Drag Reduction SMOOTH-SHIPS, Istanbul, Turkey*.
- Watanabe, O., A. Masuko and Y. Shirose (1998). Measurements of drag reduction by microbubbles using very long ship models *J. Soc. Naval Arch. Japan* 183, 53-63.
- Zverkhovskiy, O., Terwisga, R. Delfos, J. Westerweel (2013). Flat Plate Drag Reduction by an Air Cavity. *The International Conference on Advanced Measurement Technology for EU Maritime Industry, Gdansk, Poland*.
- Zverkhovskiy, O., Terwisga, R. Delfos, J. Westerweel (2012) Experimental Study on Developed Air Cavities Horizontal Flat Plate. *International Symposium on Cavitation, Singapore*.